

Article

Effect of Hydrogen Charging on the Mechanical Properties of High-Strength Copper-Base Alloys, Austenitic Stainless Steel AISI 321, Inconel 625 and Ferritic Steel 1.4511

Jens Jürgensen ^{1,*} , Andreas Frehn ², Klaus Ohla ^{2,†}, Sandra Stolz ¹  and Michael Pohl ¹

¹ Institute for Materials—Materials Testing, Ruhr-University Bochum, 44801 Bochum, Germany; stolz@wp.rub.de (S.S.); pohl@wp.rub.de (M.P.)

² Materion Brush GmbH, 70499 Stuttgart, Germany; andreas.frehn@materion.com (A.F.)

* Correspondence: juergensen@wp.rub.de

† Now retired.

Abstract: Hydrogen embrittlement (HE) poses the risk of premature failure for many metals, especially high-strength steels. Due to the utilization of hydrogen as an environmentally friendly energy source, efforts are made to improve the resistance to HE at elevated pressures and temperatures. In addition, applications in hydrogen environments might require specific material properties in terms of thermal and electrical conductivity, magnetic properties as well as corrosion resistance. In the present study, three high-strength Cu-base alloys (Alloy 25, PerforMet[®] and ToughMet[®] 3) as well as austenitic stainless AISI 321, Ni-base alloy IN 625 and ferritic steel 1.4511 are charged in pressurized hydrogen and subsequently tested by means of Slow Strain Rate Testing (SSRT). The results show that high-strength Cu-base alloys exhibit a great resistance to HE and could prove to be suitable for materials for a variety of hydrogen applications with rough conditions such as high pressure, elevated temperature and corrosive environments.

Keywords: hydrogen embrittlement; high-strength Cu-base alloys; pressure hydrogen charging; slow strain rate test; Thermal Desorption Mass Spectrometry



Citation: Jürgensen, J.; Frehn, A.; Ohla, K.; Stolz, S.; Pohl, M. Effect of Hydrogen Charging on the Mechanical Properties of High-Strength Copper-Base Alloys, Austenitic Stainless Steel AISI 321, Inconel 625 and Ferritic Steel 1.4511. *Metals* **2024**, *14*, 588. <https://doi.org/10.3390/met14050588>

Academic Editor: Jacques Huot

Received: 9 April 2024

Revised: 8 May 2024

Accepted: 14 May 2024

Published: 17 May 2024



Copyright: © 2024 by the authors. Licensee MDPI, Basel, Switzerland. This article is an open access article distributed under the terms and conditions of the Creative Commons Attribution (CC BY) license (<https://creativecommons.org/licenses/by/4.0/>).

1. Introduction

Hydrogen as an eco-friendly energy source is considered a cornerstone for meeting the climate targets stated within the “Paris Agreement” by reducing carbon dioxide emissions when used as a substitute for fossil fuels [1–5]. However, large-scale hydrogen technologies are still in the development phase since several different challenges must be addressed, such as the production and generation of sufficient amounts of pure hydrogen, hydrogen storage and transportation as well as the actual combustion processes. From a materials point of view, hydrogen poses the risk of “hydrogen embrittlement” (HE) for metals, i.e., the material’s loss of ductility when put under (elastic) stress [6–9]. This could lead to premature failure of metallic components, which not only bears the risk of machine downtimes but also of endangering human life, since hydrogen technologies often require high pressures.

The umbrella term HE covers a multitude of different failure mechanisms [10,11] which are best categorized by the respective sources of hydrogen ingress. Thus, Internal Hydrogen Embrittlement (IHE) refers to failures caused by hydrogen from manufacturing processes such as casting (pores and “fish eyes”), welding or heat treatment [8,9,12]. Damage might emerge during manufacturing or as delayed fracture when a hydrogen-containing component is put under operating stresses. Hydrogen Environmental Embrittlement (HEE) is the most common form of HE [8,9,13–15]. Hydrogen is either generated due to contact with aqueous solutions as a product of corrosion processes (cathodic stress corrosion cracking) or by a gaseous atmosphere such as pressurized hydrogen. The latter is the main source of ingress when hydrogen is used as an energy source.

Hydrogen uptake into metals by pressurized hydrogen involves several steps, which are affected by various parameters such as the surface condition of the metal and in particular the composition of the gaseous atmosphere [16,17]. The first step in this process is called physical adsorption, where hydrogen molecules (H_2) are bonded to the metal surface via van der Waals forces. Afterward, the hydrogen molecules are chemically bonded via stronger covalent bonds. The most crucial step of hydrogen uptake from gaseous atmospheres is the dissociation of H_2 molecules into two hydrogen atoms since only atomic hydrogen can be absorbed into solid metals. For this to happen, an external energy of 436.22 kJ/mol H_2 [18] is required. In technical applications, this means that a significant hydrogen uptake is only possible if the material surface is metallically blank and if the gaseous atmosphere does not contain inhibiting agents such as O_2 , CO or SO_2 [19,20]. On the other hand, species such as CO_2 and especially H_2S act as promoting agents which significantly increase the hydrogen uptake [19,21]. Only after dissociation, hydrogen atoms will enter the metal lattice (absorption). Once absorbed, hydrogen may either diffuse via interstitial lattice sites (“diffusive hydrogen”) or become trapped at different lattice defects such as grain boundaries, non-metallic inclusions/foreign phases and dislocations. Therefore, the total amount of hydrogen H_{tot} within metals equals the sum of diffusive hydrogen H_{diff} and trapped hydrogen T_{trap} :

$$H_{tot} = H_{diff} + T_{trap}$$

HE is generally caused by diffusive hydrogen [3,6–9,11,22]. By providing external activation energy in the form of elevated temperature or mechanic stresses, trapped hydrogen may become diffusive and therefore contribute to HE [9,23–26]. The required energy is dependent on the specific trapping site and ranges from around 15 kJ per mol H (e.g., dislocation cores) up to around 100 kJ per mol H (e.g., interfaces of TiC), allowing for the classification of different trapping sites [27–30].

The process of HE is explained via two main mechanisms referred to as Hydrogen-Enhanced Decohesion/HEDE and Hydrogen-Enhanced Localized Plasticity/HELP [3,7,22,31–35]. Within the literature, there are additional theories of HE [36–38] which are heavily debated [39] and probably not sufficient to solely explain all hydrogen-related effects in metals. It is most likely that HE is attributed to an interplay of different damaging mechanisms, such as HEDE and HELP [9,36,40].

The occurrence of HE is strongly dependent on the crystallographic structure and microstructure of the metal, its ultimate tensile strength, grain size, phase and precipitate distribution as well as external factors such as hydrogen content and applied stresses. BCC metals, e.g., high-strength steels, are considered susceptible to HE when exceeding an ultimate tensile strength of 800 MPa [41,42]. This is explained by very fast hydrogen diffusion velocities within BCC steels between 1.0×10^{-7} for ferritic microstructures [43] and 2.0×10^{-9} cm²/s for martensitic microstructures [44,45] as well as low hydrogen solubility. High-strength steels endure higher (elastic) operating stresses, which act as driving forces for hydrogen diffusion [3]. Therefore, hydrogen predominantly diffuses into locally strained lattice areas such as crack tips, radii, thread bases, etc. This yields a local increase in diffusive hydrogen concentrations which may ultimately exceed a material-dependent critical threshold value and therefore induce HE. This mechanism is referred to as the “Gorsky effect” [46,47].

On the other hand, FCC metals, such as stable austenitic stainless steels, generally exhibit a rather low susceptibility to HE. This is attributed to very low hydrogen diffusion coefficients of around 1.0×10^{-12} cm²/s [48] as well as their hydrogen solubility being around 100 times higher compared with BCC metals [49]. In addition, FCC metals cannot fracture due to cleavage (i.e., HEDE mechanism) since slipping planes are always activated prior to cleavage planes. Therefore, only effects attributed to HELP may occur, resulting in decreased values for elongations at fracture and reduction in area when FCC metals are mechanically tested under static or quasi-static strain rates. These effects must be evaluated

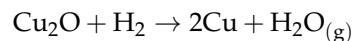
separately since most technical applications superimpose stresses well below the material's yield strength, which usually remains unaffected by hydrogen in FCC metals.

Several research papers indicate that for austenitic stainless steels, the resistance to HE increases with the stabilizing of the FCC phase [50–54]. Therefore, both a low M_{d30} temperature as well as high stacking fault energies above 43 mJ/m² improve the resistance to HE since the FCC is stabilized and the formation of deformation twins is postponed.

However, metastable austenitic stainless steels exhibit a certain susceptibility to HE, predominantly when strain-induced martensite (BCC phase) is formed due to machining, operation stresses or deep-freezing [55,56]. In terms of high-pressure hydrogen applications, these materials are not suitable.

Some applications, such as power generation, chemical production, oil refineries or direct combustion (e.g., fuel cells) require a multitude of different material properties. Among others, these include high tensile strength, good corrosion resistance, high thermal and electric conductivities, high resistance to biofouling, non-magnetic properties, low hydrogen permeation rates, etc. Taking these requirements into consideration, high-strength copper alloys may prove as applicable materials. However, little to no data are available for copper-based alloys, especially high-strength precipitation-hardened alloys, in terms of their susceptibility to HE.

It is known that oxygen-containing copper may suffer from the so-called “hydrogen illness” [57,58]. In particular, this failure mechanism occurs when copper is soldered or welded within hydrogen-containing shielding gas. Due to the elevated temperature, reaction kinetics are fast and therefore hydrogen from the shielding gas may react with the copper-oxygen-eutectic (Cu₂O) which is mainly located at the grain boundaries, according to the following equation:



The generation of water vapor yields the formation of linear porosity (preferably at the grain boundaries) within the softened copper, resulting in severe inner defects that may cause cracking. The mechanism of “hydrogen illness” is completely avoided when Oxygen Free Copper (OFC) is used. Due to its decreased oxygen content of 10 ppm and below, the formation of Cu₂O is reduced to a minimum and thus the formation of pores is suppressed.

Yamabe et al. investigated a high-strength precipitation-hardened copper-beryllium alloy with an ultimate tensile strength of around 1400 MPa with respect to its susceptibility to HE [59]. Both notched and un-notched samples were charged in 115 MPa (1150 bar) pressurized hydrogen at room temperature with subsequent mechanical testing by means of Slow Strain Rate Tests (SSRT). The results did not show any effect of hydrogen on the mechanical properties; therefore, no HE was present. The authors contribute these findings to the low hydrogen solubility of copper as well as the low hydrogen diffusion coefficient. They measured a hydrogen solubility of 0.1 mol H₂/(m³MPa^{1/2}) and a hydrogen diffusion coefficient of 1.0 × 10^{−10} m²/s, both at around 300 °C. The results are in good agreement with several other works performed on varying copper alloys [60–64].

In the present work, different high-strength copper alloys were charged in pressurized hydrogen at elevated temperatures and subsequently tested by Slow Strain Rate Tests (SSRT). Hydrogen contents were measured by Thermal Desorption Spectroscopy (TDS) and fracture surfaces were investigated in a scanning electron microscope (SEM). The results are compared to hydrogen-free reference samples as well as corrosion-resistant ferritic steels, austenitic stainless steels and nickel-based alloys.

2. Materials and Methods

2.1. Investigation Materials

In this study, three different high-strength Cu-base alloys were investigated. The materials were provided by Materion Brush GmbH (Stuttgart, Germany). Care was taken to ensure that the same semi-finished product (here, the rod material) was used in a similar

dimensional range. Sample material was taken from serial production, and no additional process steps or treatments were performed.

Beryllium-containing Alloy 25 (material A, UNS standard C17200) is a solution-annealed and age-hardened high-strength alloy, surpassing any other commercial Cu alloy in terms of ultimate tensile strength. Age hardening is realized by the precipitation of γ -phase and finely dispersed CuBe_2 . Due to the material's exceptional resistance to stress relaxation at elevated temperatures and its high fatigue strength, it is often used for springs in elevated temperature applications. Other applications include bushings, sub-sea components or tooling inserts.

PerforMet[®] (material B) is a Beryllium-free solution annealed alloy, aged hardened by the precipitation of nickel-silicide (Ni_2Si). The material exhibits a high thermal conductivity as well as great wear and corrosion resistance and a decreased tendency of galling. Applications include valve seats, valve guides, piston rings and plain bearings. It is also used for fast-cycle injection mold components.

ToughMet[®] 3 (material C, UNS standard C96970) is a spinodally hardened Cu-Ni-Sn alloy with strength and hardness equivalent to Alloy 25 but without the addition of Beryllium. The material exhibits an exceptional tarnish resistance at room temperature and high corrosion resistance surpassing Alloy 25. It is mainly used for heavily loaded bushings or bearings commonly found in aircraft, off-road equipment and industrial machinery. It can also be used in sour oilfield service.

In addition to the aforementioned Cu-base alloys, two Fe-base alloys and one Ni-base alloy were investigated.

Austenitic stainless steel AISI 321 (material D, 1.4541, X6CrNiTi18-10) exhibits good corrosion resistance. Due to the addition of Ti and the formation of around 5% of delta-ferrite within the matrix, the tendency of intergranular corrosion is suppressed so that the material is classified as weldable.

Ni-base alloy IN 625 (material E, 2.4856, UNS N06625) was investigated in grade 1 condition (soft annealed) with exceptional resistance to a wide range of corrosive environments combined with an elevated strength level. The latter is derived from the addition of Nb and Mo and therefore solid solution strengthening. IN 625 is typically used in sea-water applications, in facilities for processing nuclear waste as well as facilities for producing highly aggressive acids.

Finally, ferritic steel 1.4511 (material F, X3CrNb17) represents a moderately corrosion-resistant steel with a BCC lattice. The material is magnetic and weldable (though, grain growth must be avoided), with additions of Nb improving the resistance to intergranular corrosion. Applications include solenoid valves, sensors and injection valves.

This section may be divided by subheadings. It should provide a concise and precise description of the experimental results, their interpretation, as well as the experimental conclusions that can be drawn.

The nominal chemical composition of all investigated materials is listed in Table 1. Light-microscopic micrographs are presented in Figure 1.

Table 1. Nominal chemical composition of all investigated materials. * According data sheets provided by Materion Brush GmbH. ** According to DIN EN 10088-3 [65]. *** According to VdTÜV data sheet 499.

| ID | Material | wt % | | | | | | |
|----|---------------------------|------|-----------|-------|---------|-----------|---------|----|
| | | Base | Be | Ni | Co | Si | Cr | Sn |
| A | Alloy 25 * | Cu | 1.8–2.0 | > 0.2 | | | | |
| B | PerforMet [®] * | | 6.5–7.5 | | 1.5–2.0 | 0.75–1.25 | | |
| C | ToughMet [®] 3 * | | 14.5–15.5 | | | | 7.5–8.5 | |

Table 1. Cont.

| | | Non-Cu materials | | | | | | |
|-----|-------------|------------------|-----------|------|----------|-----------|----------|-----------|
| ID. | Material | wt % | | | | | | |
| | | Base | C | Si | Mn | Cr | Ni | Ti |
| D | AISI 321 ** | Fe | ≤0.08 | ≤1.0 | ≤2.0 | 17.0–19.0 | 9.0–12.0 | 5 × C |
| ID. | Material | wt % | | | | | | |
| | | Base | Cr | Fe | Mo | Nb + Ta | Mn | Co |
| E | IN 625 *** | Ni | 21.0–23.0 | ≤5.0 | 8.0–10.0 | 3.2–4.2 | ≤0.50 | ≤1.0 |
| ID. | Material | wt % | | | | | | |
| | | Base | C | Si | Mo | Cr | Ni | Nb |
| F | 1.4511 ** | Fe | ≤0.03 | ≤1.0 | ≤1.0 | 16.0–18.0 | - | 0.20–0.50 |

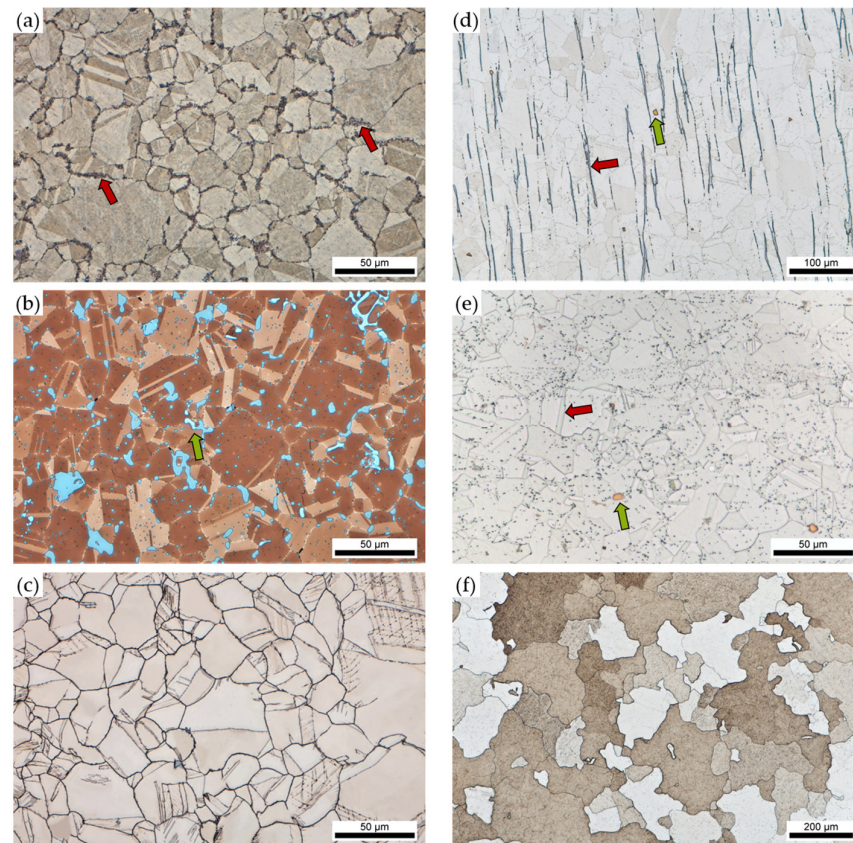


Figure 1. Micrographs of all investigated materials. (a) Alloy25. Arrow: Gamma phase. (b) PerforMet[®]. Arrow: Ni₂Si (nickel silicide). (c) ToughMet[®] 3. (d) AISI 321. Red arrow: delta ferrite, green arrow: TiN (titanium nitride). (e) IN 625. Red arrow: annealing twins, green arrow: TiN. (f) 1.4511.

2.2. Sample Geometry

All samples for mechanical testing and hydrogen analyses were machined according to Figure 2. Within the gauge length, the surface was precision turned with an average roughness Ra of 6.3 μm. In comparison to standard DIN 50125:2022-08 [66], the radius within the transition from the threaded sample head to the gauge length was increased to prevent hydrogen-induced fractures in this area due to a local stress increase.

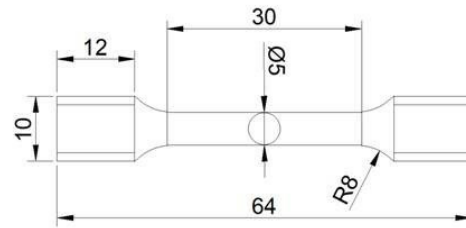


Figure 2. Sample geometry for mechanical testing and hydrogen analyses (Unit: mm).

2.3. Hydrogen Charging

Hydrogen charging was carried out in a pressure autoclave with 6.0 high-purity hydrogen ($\geq 99.9999\%$). The charging parameters are summarized in Table 2. Charging was conducted until a homogenous hydrogen distribution was reached within the gauge length of the tensile test samples. The required minimum charging durations were calculated based on the respective hydrogen diffusion coefficients of each material, with $D = 6 \times 10^{-6} \text{ m}^2/\text{s}$ for the copper alloys [67], $D = 8.9 \times 10^{-7} \text{ m}^2/\text{s}$ for AISI 321 [67,68], $D = 4.8 \times 10^{-7} \text{ m}^2/\text{s}$ for IN 625 [67] and $D = 6.40 \times 10^{-9} \text{ m}^2/\text{s}$ for 1.4511 [67].

Table 2. Parameters of pressure hydrogen charging.

| No. | Material | Charging Duration | Hydrogen Pressure | Temperature |
|-----|-------------------------|-------------------|-------------------|-------------|
| A | Alloy 25 | | | |
| B | PerforMet [®] | 21 days | 275 bar/27.5 MPa | 573 K |
| C | ToughMet [®] 3 | | | |
| D | AISI 321 | 28 days | 45 bar/4.5 MPa | 623 K |
| E | IN 625 | 14 days | 60 bar/6 MPa | 673 K |
| F | 1.4511 | 21 days | 275 bar/27.5 MPa | 573 K |

Between venting of the pressure autoclaves and cooling of the samples, a maximum period of 20 min elapsed.

After charging, all samples were stored within a liquid nitrogen container to prevent hydrogen effusion. An exception was made for austenitic stainless steel AISI 321 since the formation of martensite was expected due to deep freezing. This material was stored in a freezer at $-18 \text{ }^\circ\text{C}$ (255.15 K) for a maximum of 7 days after charging.

2.4. Reference Thermal Exposure Tests

Since hydrogen charging was conducted at elevated temperatures, microstructural changes in the precipitation-hardened high-strength Cu alloys must be assessed. To account for the influence of the charging temperature, reference exposure tests were performed for each Cu alloy. In this step, samples were heated in a furnace to 573 K in an ambient atmosphere. The temperature was held isothermally for 21 days (equaling the charging duration). Therefore, no hydrogen charging took place. These samples were used as additional references during SSRT, to assess temperature-related effects on the mechanical properties.

2.5. Hydrogen Analyses

Hydrogen analyses were carried out by means of Thermal Desorption Mass Spectrometry (TDMS) in a Bruker IR 07 equipped with a Quadrupole mass analyzer (Figure 3). Prior to analysis, the cooled samples were thawed in 99.9% ethanol for 2 min and subsequently dried. The analyzing temperature of $300 \text{ }^\circ\text{C}$ (573 K) was reached by applying the maximum heating rate with a subsequent isothermal holding step until all hydrogen was detected. Temperature measurements were conducted by a thermocouple attached to the samples. By applying this method, the diffusive hydrogen content within the samples was analyzed.

Since HE is primarily caused by diffusive hydrogen, trapped hydrogen was not specifically determined within the scope of this investigation.



Figure 3. Thermal Desorption Mass Spectroscopy (TDMS).

2.6. Mechanical Testing

Mechanical testing was conducted by means of Slow Strain Rate Tests (SSRT) both on uncharged reference samples and hydrogen-charged samples. Due to the homogeneous hydrogen distribution profile within the charged samples, strain rates of 0.075 mm/min were chosen for all SSRT. The elongation at fracture was measured by a mechanical extensometer which was kept attached to the samples until fracture.

Since testing was carried out in a natural atmosphere, one broken fragment of each sample was immediately stored in liquid nitrogen after fracturing to analyze the remaining hydrogen content. These results were used as proof that no significant amounts of hydrogen effused out of the samples during SSRT. The other fragment was fractographically investigated in the SEM to assess the influence of hydrogen on the fracture mode and the fracture pattern.

The effect of hydrogen charging on the mechanical properties was quantified by calculating the hydrogen embrittlement indexes relative reduction in area (RRA) and relative elongation at fracture (REI), according to the following equations:

$$RRA = \frac{RA_{H \text{ charged}}}{RA_{\text{uncharged}}}$$

$$REI = \frac{El_{H \text{ charged}}}{El_{\text{uncharged}}}$$

3. Results

3.1. Hydrogen Analyses

The results of Thermal Desorption Analyses are summarized in Table 3.

For Cu base alloys Alloy 25 and PerforMet[®], no significant hydrogen uptake was found. However, the ToughMet[®] 3 material exhibited an increased hydrogen content of around 4.5 ppm.

AISI 321 (27 ppm) and IN 625 (17 ppm) contained significant amounts of hydrogen. In ferritic steel 1.4511 around 0.9 ppm diffusive hydrogen were present.

During Slow Strain Rate Testing, only negligible hydrogen effusion has occurred, ensuring that all results can be referenced to the initial hydrogen content after charging.

Table 3. Results of Thermal Desorption Analyses. * Resolution limit.

| No. | Material | Initial Hydrogen Content in ppm | Hydrogen Content after Charging in Mass ppm | Hydrogen Content after SSRT in Mass ppm |
|-----|-------------------------|---------------------------------|---------------------------------------------|-----------------------------------------|
| A | Alloy 25 | <0.001 * | 0.02 ± 0.02 | 0.02 ± 0.02 |
| B | PerforMet [®] | <0.001 * | 0.07 ± 0.03 | 0.08 ± 0.04 |
| C | ToughMet [®] 3 | <0.001 * | 4.50 ± 0.11 | 4.46 ± 0.09 |
| D | AISI 321 | 0.89 ± 0.1 | 26.8 ± 0.9 | 26.2 ± 0.7 |
| E | IN 625 | 0.1 ± 0.05 | 17.7 ± 0.7 | 17.1 ± 0.8 |
| F | 1.4511 | 0.02 ± 0.01 | 0.85 ± 0.08 | 0.79 ± 0.12 |

3.2. Mechanical Testing and Fractography

The results of all SSRT alongside with fractographic investigations of each reference sample and hydrogen-charged sample are shown in Figures 4–9.

For material Alloy 25 (Material A, Figure 4), both the hydrogen-free reference samples and the thermally exposed samples exhibit the same mechanical properties, meaning that no significant aging effect has occurred during pressure hydrogen charging. Compared to the hydrogen-free reference samples, no significant effect on the mechanical properties was found for the charged samples. The elongation at fracture tends to be slightly decreased but all samples fractured well within the plastic region of the stress–strain curves, but no severe effect of HE occurred.

These findings are backed up by the fractographic investigations. The hydrogen-free reference sample (a–c) exhibits a ductile fracture pattern consisting of both trans- and intergranular dimples (b). The dimple collars are distinctly extracted underlining the overall ductile fracture behavior (c). The fracture pattern of the hydrogen-charged samples (d–f) is nearly identical to the uncharged samples. However, within the intergranular areas, the dimples' collars are slightly shallower (f), indicating marginally less plastic deformation during the SSRT. These findings most likely have contributed to the slight decrease in elongation at the fracture of the charged samples. Other effects of hydrogen on the fracture pattern were not found for Alloy 25.

Material B, PerforMet[®] (Figure 5) was not affected by temperature exposure, either. The mechanical properties of both the hydrogen-free reference samples and the thermally exposed samples are identical, meaning that no aging effect has occurred.

However, the effect of hydrogen charging on the mechanical properties appears to be a bit more pronounced compared with material A, Alloy 25. The average elongation at fracture is reduced by around 1%.

Fractography of the uncharged reference samples revealed a transgranular fracture pattern with an overall ductile dimple fracture type (a–c). In accordance with the material's chemical composition, there are several Ni- and Si-rich precipitations of type Ni₂Si (nickel silicide) present. The fractographic investigation of the charged sample (d–f) did not reveal hydrogen-induced fracture patterns. The fracture appearance does not differ from the uncharged sample. Interfaces of Ni₂Si precipitates could act as local fracture initiation sites due to their trapping behavior and the related increased local hydrogen content. However, none of the Ni₂Si precipitates distinctly initiated failure.

Material C, ToughMet[®] 3 (Figure 6), was affected by temperature exposure. Compared to the reference samples, the thermally exposed samples suffer from a considerable loss in elongation at fracture of around 30%. Both the yield strength and ultimate tensile strength increased by around 50 MPa. The effects are most likely contributed to the solid solution hardening. Therefore, the mechanical properties of the hydrogen-charged samples are subsequently compared to the exposed samples.

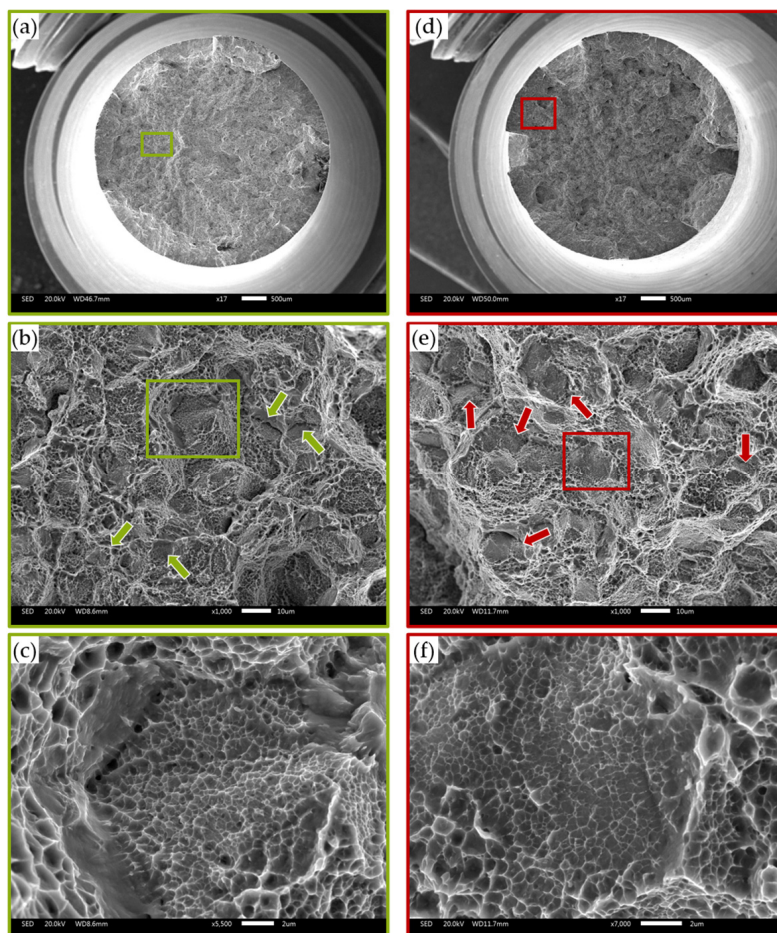
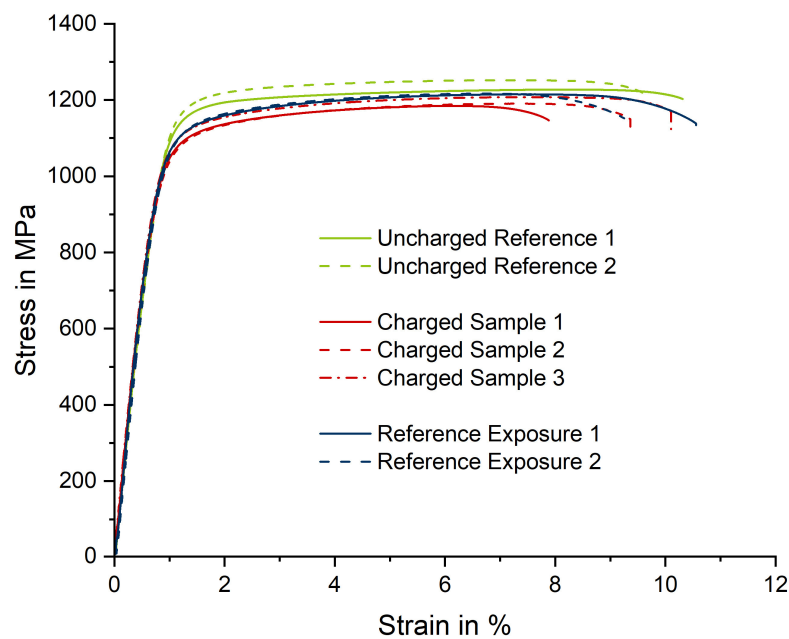


Figure 4. Alloy 25: Results of SSRT and fractographic investigations. **(Left)** (green frames): Uncharged reference sample 1. **(Right)** (red frames): Hydrogen-charged sample 2. Green and red arrows: Intergranular fracture. **(a)** Uncharged sample 1, overview, **(b)** Magnification of the green frame in **(a)**, **(c)** Magnification of the green frame in **(b)**, **(d)** Charged sample 2, overview, **(e)** Magnification of the red frame in **(d)**, **(f)** Magnification of the red frame in **(e)**.

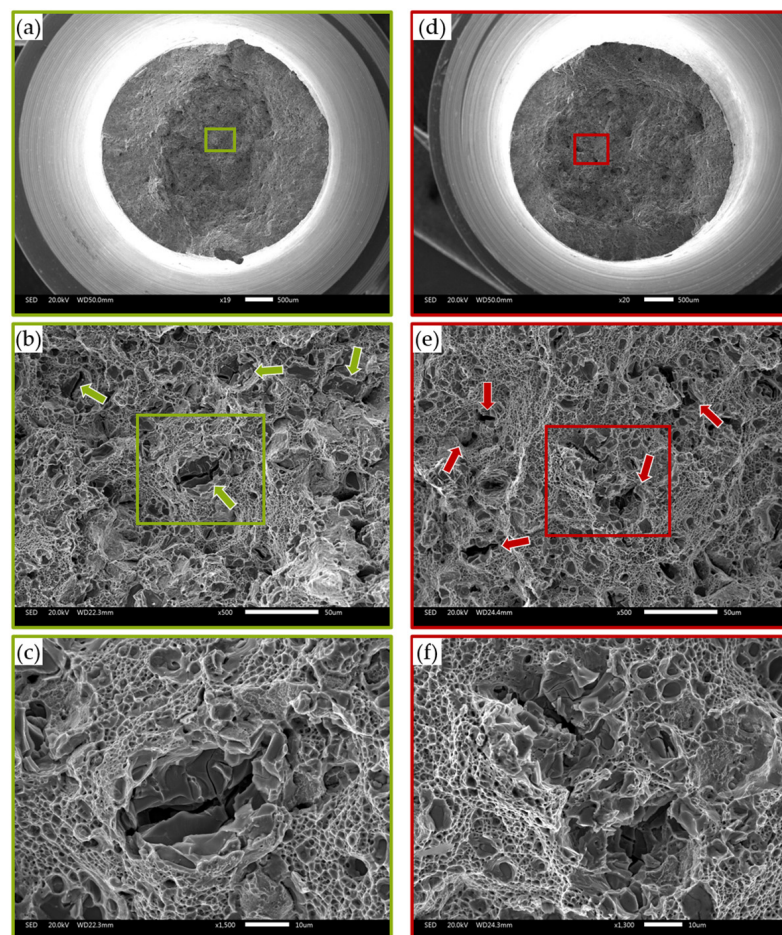
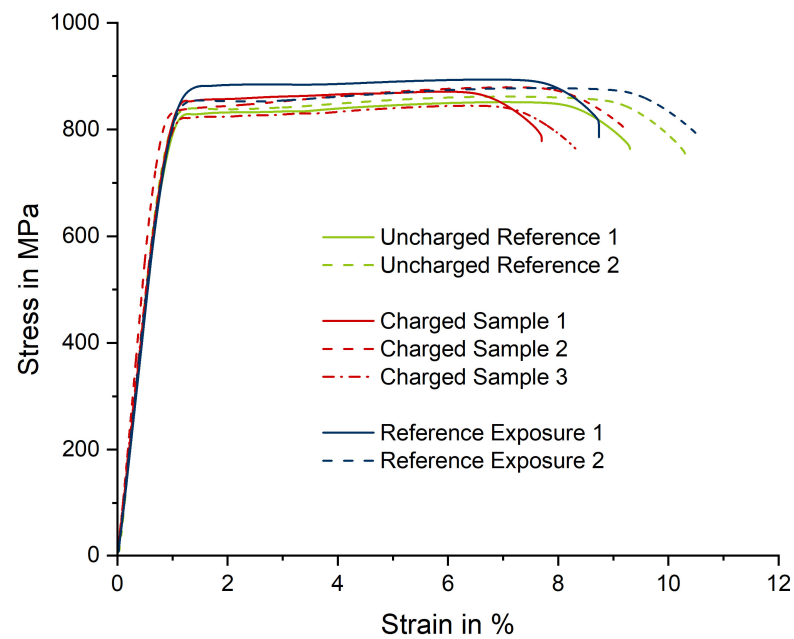


Figure 5. PerforMet[®]: Results of SSRT and fractographic investigations. **(Left)** (green frames): Uncharged reference sample 1. **(Right)** (red frames): Hydrogen-charged sample 2. Green and red arrows: Ni₂Si, nickel silicides. **(a)** Uncharged sample 1, overview, **(b)** Magnification of the green frame in **(a)**, **(c)** Magnification of the green frame in **(b)**, **(d)** Charged sample 2, overview, **(e)** Magnification of the red frame in **(d)**, **(f)** Magnification of the red frame in **(e)**.

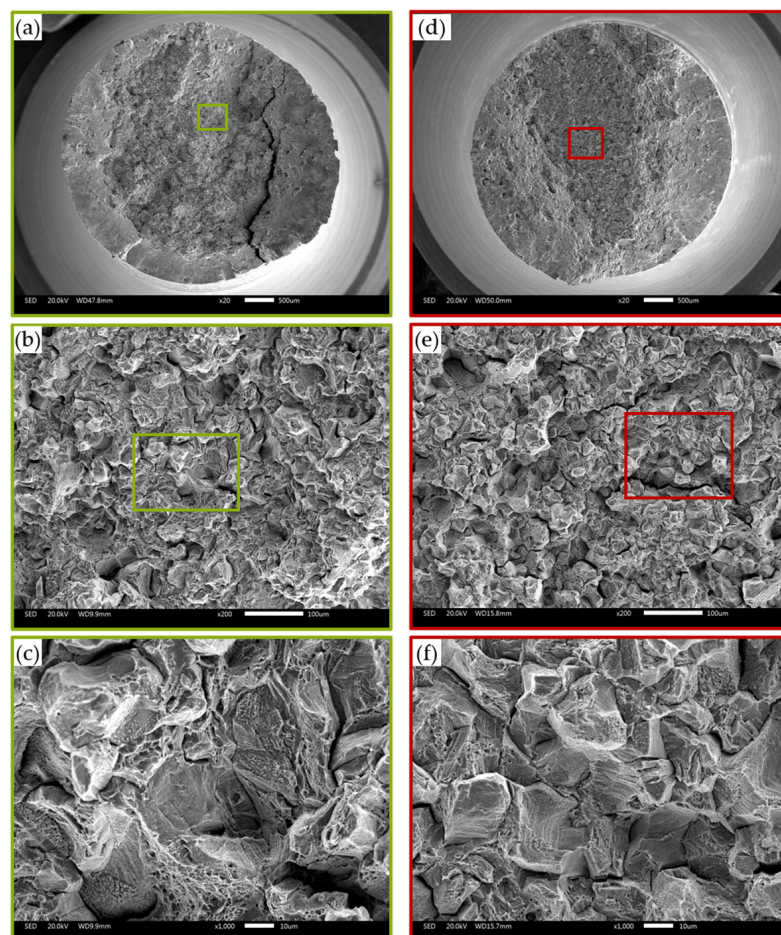
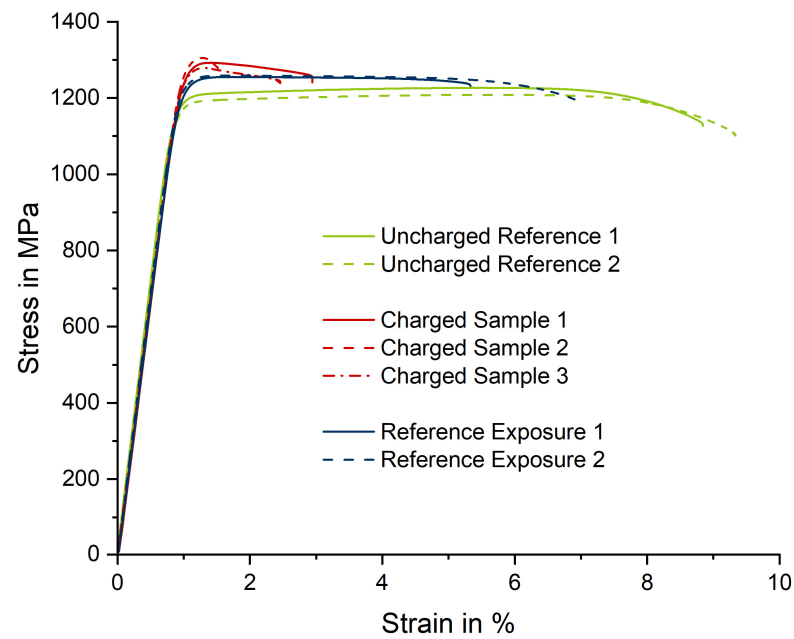


Figure 6. ToughMet[®] 3: Results of SSRT and fractographic investigations. **(Left)** (green frames): Uncharged reference exposure sample 2. **(Right)** (red frames): Hydrogen-charged sample 2. **(a)** Uncharged sample 2, overview, **(b)** Magnification of the green frame in **(a)**, **(c)** Magnification of the green frame in **(b)**, **(d)** Charged sample 2, overview, **(e)** Magnification of the red frame in **(d)**, **(f)** Magnification of the red frame in **(e)**.

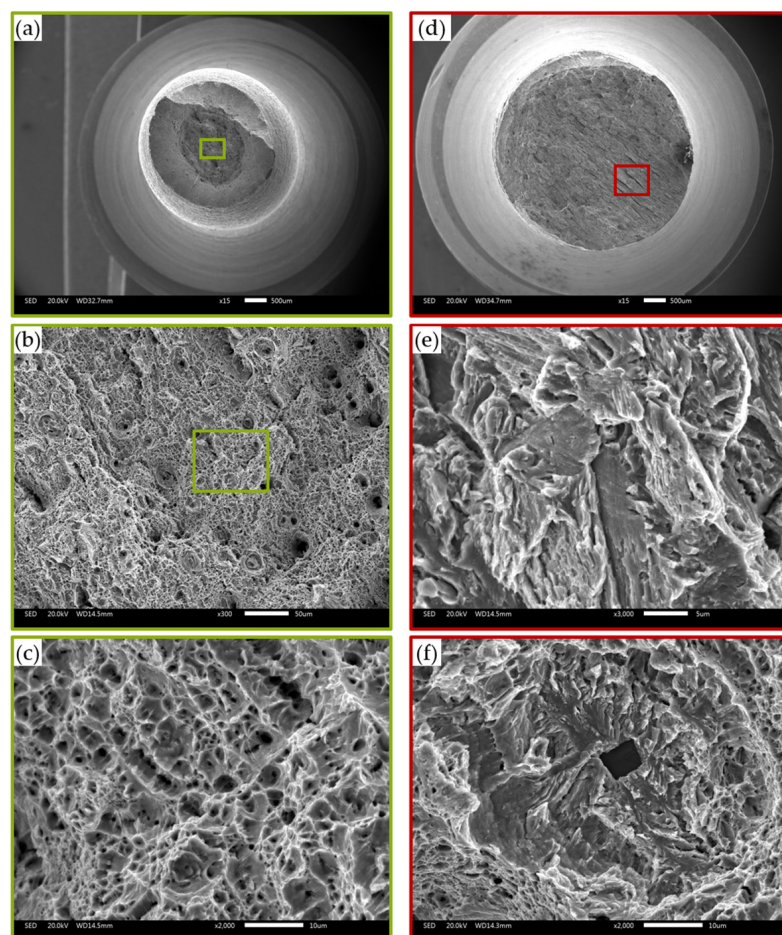
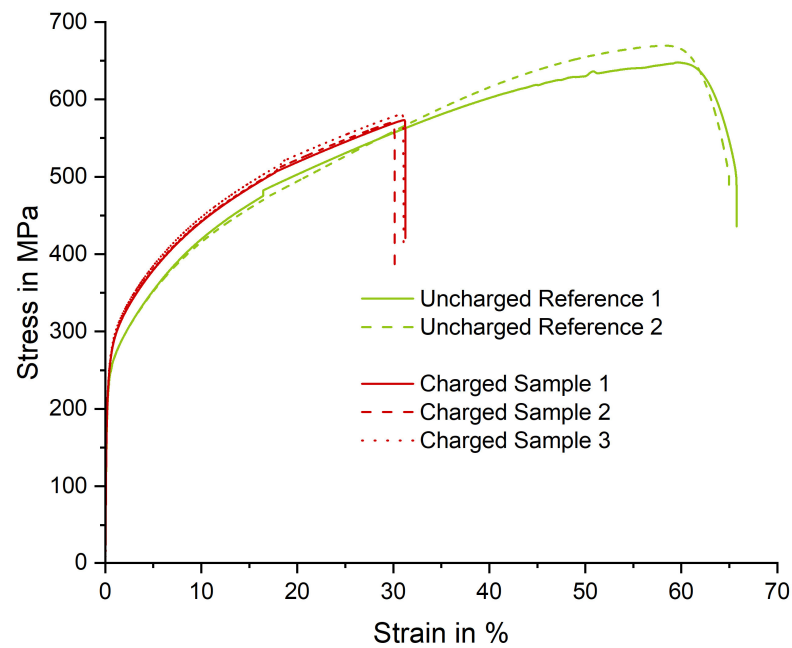


Figure 7. AISI 321: Results of SSRT and fractographic investigations. **(Left)** (green frames): Uncharged reference sample 2. **(Right)** (red frames): Hydrogen-charged sample 1. **(a)** Uncharged sample 2, overview, **(b)** Magnification of the green frame in **(a)**, **(c)** Magnification of the green frame in **(b)**, **(d)** Charged sample 2, overview, **(e)** Magnification of the red frame in **(d)**, **(f)** Different spot within the red frame in **(d)**.

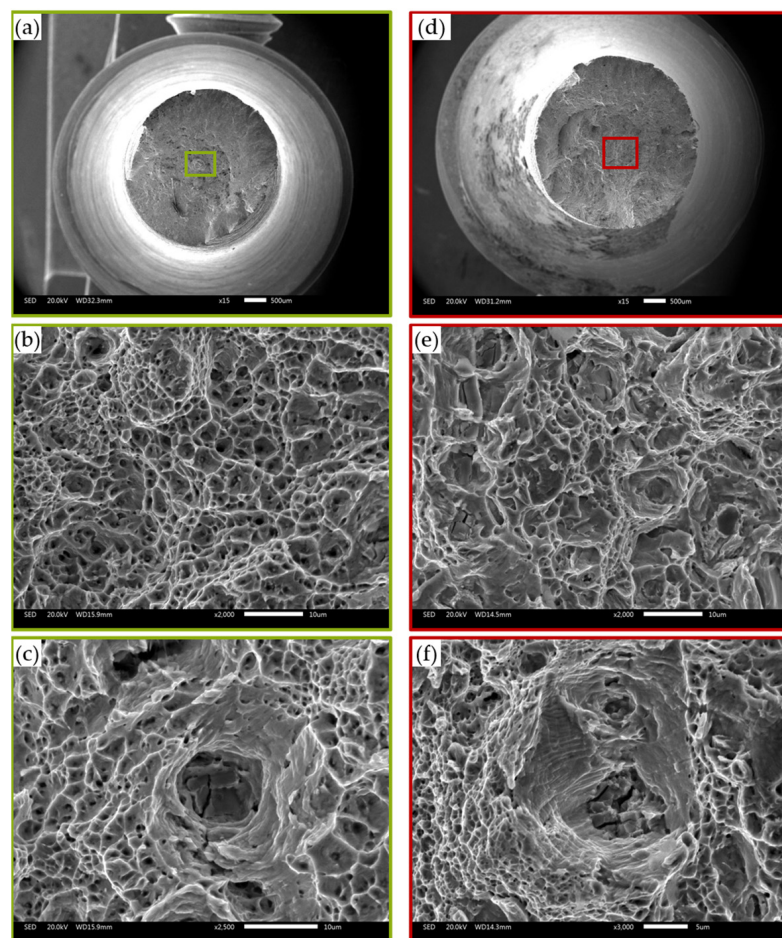
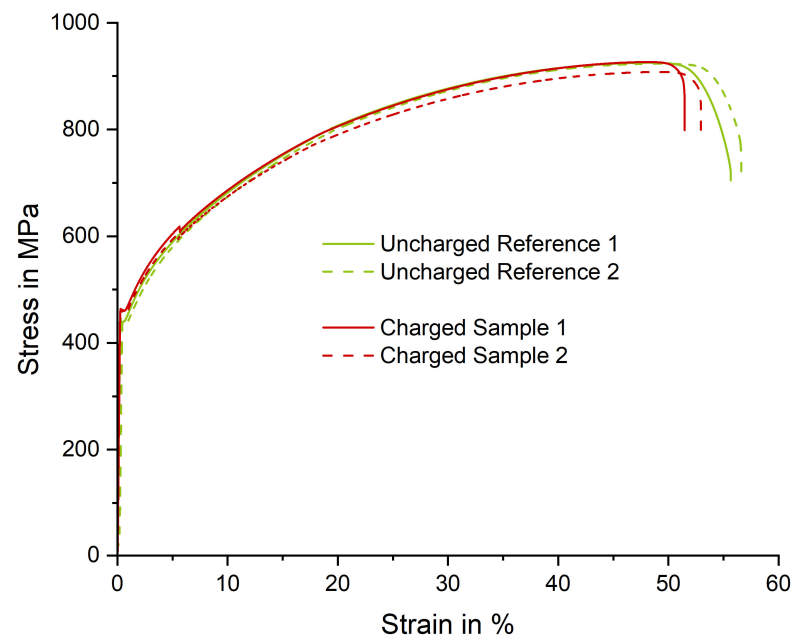


Figure 8. IN 625: Results of SSRT and fractographic investigations. **(Left)** (green frames): Uncharged reference sample 1. **(Right)** (red frames): Hydrogen-charged sample 2. **(a)** Uncharged sample 1, overview, **(b)** Magnification of the green frame in **(a)**, **(c)** Different spot within the green frame in **(b)**, **(d)** Charged sample 2, overview, **(e)** Magnification of the red frame in **(d)**, **(f)** Different spot within the red frame in **(e)**.

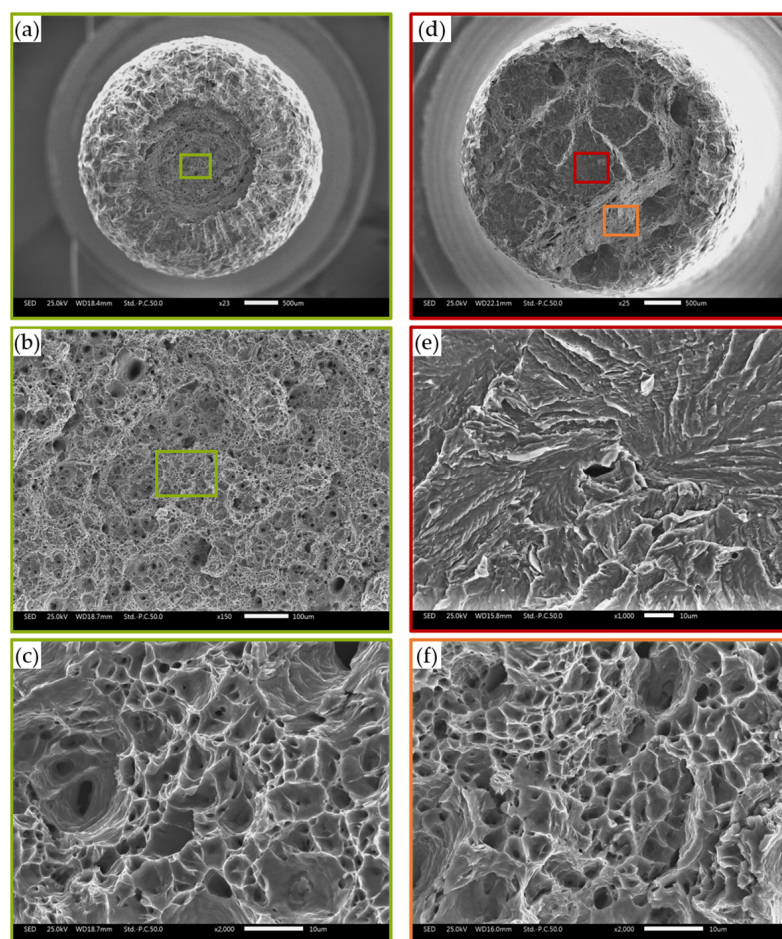
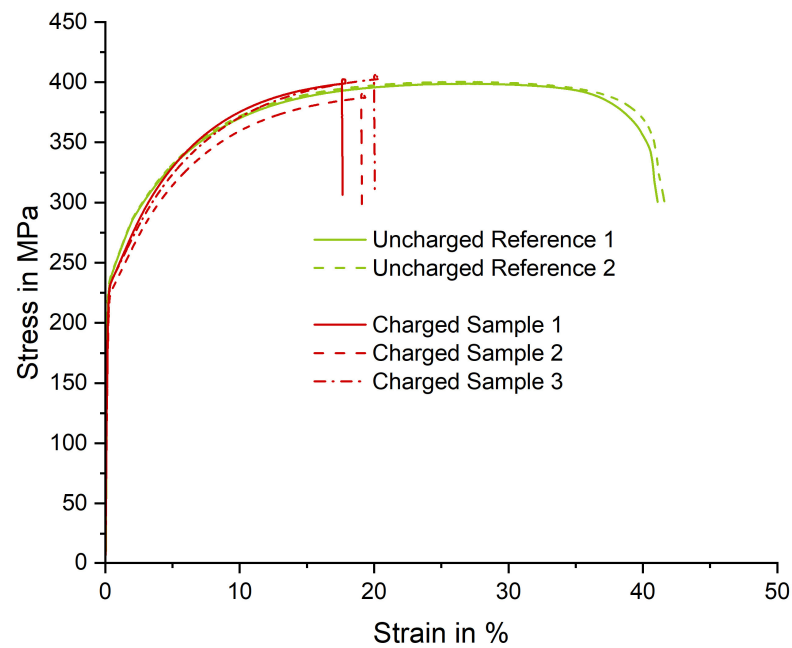


Figure 9. 1.4511: Results of SSRT and fractographic investigations. **(Left)** (green frames): Uncharged reference sample 2. **(Right)** (red and orange frames): Hydrogen-charged sample 2. **(a)** Uncharged sample 2, overview, **(b)** Magnification of the green frame in **(a)**, **(c)** Magnification of the green frame in **(b)**, **(d)** Charged sample 2, overview, **(e)** Magnification of the red frame in **(d)**, **(f)** Magnification of the orange frame in **(d)**.

After hydrogen charging the elongation at fracture is even more reduced compared to the hydrogen-free samples. The relative decrease is around 60% resulting in an absolute value of around 1.5%. Therefore, only small amounts of plastic deformation occur prior to the fracture of the samples.

The fracture surface of the uncharged samples predominantly exhibits an intergranular structure with some transgranular patterns (a and b). Several dimples are visible, of which some are quite shallow while others have distinctly deformed collars (c). Within the intergranular areas, there are slip lines visible. The overall fracture appearance of the charged sample (c and e) is similar to the uncharged samples. However, higher magnifications reveal that more pronounced localized slipping has occurred in the intergranular areas and the dimple's morphology is even shallower (f). Localized slipping is most likely attributed to the HELP mechanism.

Austenitic stainless steel AISI 321 (Figure 7) suffered from a significant loss of ductility in the hydrogen-charged condition. The uncharged reference sample exhibits a ductile dimple fracture throughout the whole fracture surface (a–c). Significant necking of the sample is visible (a). On the other hand, the charged sample's degree of necking is considerably reduced (d). The fracture changed to a “feathery” type (e). The effect is predominantly visible near interfaces between delta-ferrite and the surrounding matrix as well as near non-metallic inclusions of type TiC. Here, typical forms of “fish eyes” were present in high quantities (f). “Feathery” fractures are typically found on low- to medium-strength BCC steels in a hydrogen-charged condition, indicating that AISI 321 may have suffered from a severe formation of strain-induced martensite during SSRT.

Similar to Alloy 25 and PerforMet[®], Ni-base alloy IN 625 (Figure 8) was not severely affected by hydrogen charging, either. Both the fracture surfaces of hydrogen-free reference samples (a–c) and the charged samples (d–f) exhibit an overall ductile behavior. The fracture pattern is dominated by fracture dimples with distinctly extracted collars and thus high plastic deformation. In the vicinity of non-metallic inclusions of type TiC, more pronounced localized slipping occurred after hydrogen charging (f). This effect becomes evident by distinct slip lines and deep collars around TiC. Other than that, changes in fracture morphology due to hydrogen charging were not found.

Finally, ferritic steel 1.4511 (Figure 9) was also significantly affected by hydrogen, resulting in a relative loss of elongation at fracture of around 15%.

Fractographic investigations proved an even more severe effect of hydrogen charging. The hydrogen-free reference samples (a–c) exhibit pronounced necking with a thoroughly ductile fracture surface consisting of dimples. On the charged samples (d–f) significantly less necking occurred (e) and wide-spread areas with a “feathery” type fracture, similar to the aforementioned samples made of AISI 321, were found (e). This fracture mode is characteristic of hydrogen-induced cracking in low- to medium-strength steels such as the investigated 1.4511. Only a small final fracture was present. Here, the fracture still appeared as a ductile dimple fracture (f).

3.3. Hydrogen Embrittlement Indexes

The mechanical properties of all samples are summarized in Table 4. Based on the reduction in area (Z) and the elongation at fracture (A), the hydrogen embrittlement indexes RRA and REI were calculated in Table 5 and plotted as a bar diagram in Figure 10.

The highest values for RRA and REI and therefore the best resistance to hydrogen embrittlement were found for high-strength Cu alloy Alloy 25 (material A). For this alloy, the calculated value for RRA (theoretically) exceeds 100% which corresponds to no HE effects whatsoever, but rather represents statistic deviations of the mechanical properties. The slightly reduced REI is caused by a single outlier sample. These findings are in accordance with the low hydrogen content within the charged samples (0.02 ppm) and the fracture surfaces which revealed hardly any difference between the hydrogen-free and hydrogen-charged samples in terms of fracture morphology.

Table 4. Results of SSRT on uncharged and hydrogen-charged samples. In brackets: mechanical properties of reference samples (heat-exposed but not charged). YS: yield strength, UTS: ultimate tensile strength, Z: reduction in area, A: elongation at fracture.

| ID | Material | Uncharged | | | | Hydrogen-Charged | | | |
|----|-------------|------------|------------|----------|-----------|------------------|----------|--------|---------|
| | | YS | UTS | Z | A | YS | UTS | Z | A |
| | | in MPa | in MPa | in % | in % | in MPa | in MPa | in % | in % |
| A | Alloy 25 | 1100 ± 13 | 1237 ± 10 | 15 ± 1 | 9 ± 0.4 | 977 ± 9 | 1137 ± 9 | 17 ± 1 | 8 ± 1 |
| | | (991 ± 13) | (1158 ± 1) | (21 ± 0) | (9 ± 0.5) | | | | |
| B | PerforMet® | 817 ± 3 | 857 ± 6 | 25 ± 3 | 9 ± 0.5 | 856 ± 11 | 821 ± 13 | 23 ± 1 | 8 ± 1 |
| | | (840 ± 9) | (886 ± 9) | (21 ± 0) | (9 ± 1) | | | | |
| C | ToughMet® 3 | 1185 ± 8 | 1218 ± 10 | 23 ± 1 | 8 ± 0.3 | 1320 ± 11 | 1330 ± 9 | 8 ± 1 | 1 ± 0.6 |
| | | (1276 ± 3) | (1295 ± 4) | (16 ± 2) | (5 ± 1) | | | | |
| ID | Material | Uncharged | | | | Hydrogen-Charged | | | |
| | | YS | UTS | Z | A | YS | UTS | Z | A |
| | | in MPa | in MPa | in % | in % | in MPa | in MPa | in % | in % |
| D | AISI 321 | 223 ± 9 | 647 ± 23 | 68 ± 1 | 66 ± 1 | 256 ± 3 | 574 ± 4 | 19 ± 1 | 31 ± 1 |
| E | IN 625 | 440 ± 2 | 925 ± 2 | 55 ± 1 | 56 ± 1 | 453 ± 3 | 909 ± 11 | 49 ± 1 | 52 ± 1 |
| F | 1.4511 | 238 ± 2 | 399 ± 2 | 85 ± 1 | 39 ± 1 | 234 ± 1 | 400 ± 7 | 42 ± 1 | 20 ± 1 |

Table 5. Hydrogen embrittlement indexes RRA and REL.

| ID | Material | RRA—Relative Reduction of Area in % | REL—Relative Elongation in % |
|----|-------------|-------------------------------------|------------------------------|
| A | Alloy 25 | 113.3 | 88.9 |
| B | PerforMet® | 92.0 | 84.4 |
| C | ToughMet® 3 | 34.8 | 19.0 |
| D | AISI 321 | 34.5 | 47.0 |
| E | IN 625 | 89.1 | 92.9 |
| F | 1.4511 | 49.4 | 51.3 |

For the Cu-base alloy PerforMet® (material B), only a minor decrease in the reduction in the area was found (RRA = 92%). However, a slightly more pronounced effect on the elongation at fracture was present (REL = 84%). Since the hydrogen contents within these samples were very low (0.07 ppm) and no significant change in fracture appearance was found, PerforMet® offers good resistance to HE, as well.

The high-strength alloy ToughMet® 3 (material C) showed a more significant effect of hydrogen on the mechanical properties. Both RRA (35%) and REL (19%) prove that the material only endures small amounts of plastic deformation until hydrogen-induced fractures occur. However, no failure below the material's yield strength was found. These findings correspond with the hydrogen content of 4.5 ppm, which is significantly higher compared to the previously discussed high-strength Cu-base alloys (materials A and B). Consequentially, the fracture surface of the charged samples revealed less plastic deformation and pronounced localized slipping which is explained by the HELP mechanism.

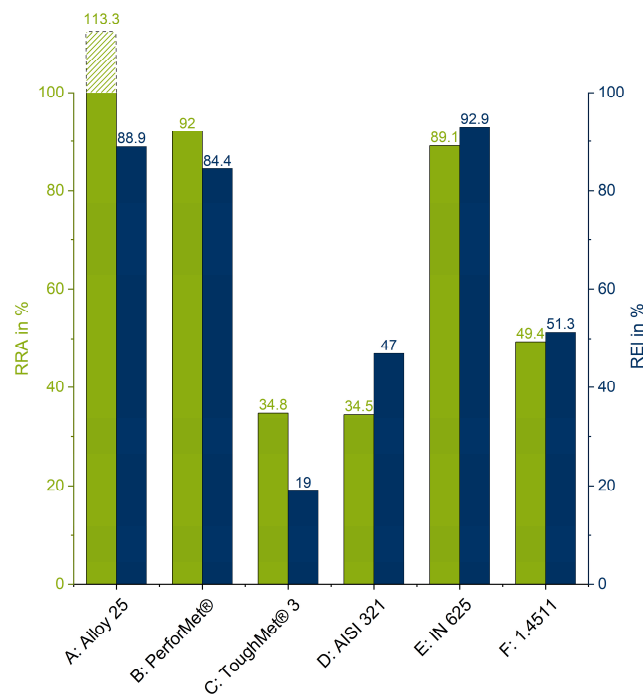


Figure 10. Graphic visualization of hydrogen embrittlement indexes RRA and REI.

Austenitic stainless steel AISI 321 also exhibits significantly reduced values for RRA (35%) and REI (47%). Despite the reduced ability to deform plastically, there was also a noticeable increased yield strength (223 MPa without hydrogen, 256 MPa after hydrogen charging). Therefore, hydrogen as an interstitial element caused solid solution strengthening in this alloy. The results agree with both the hydrogen analyses (22.3 ppm) and the fractographic investigations. The latter revealed a significant change in fracture mode from a ductile dimple fracture on the uncharged samples to a “feathery-like” structure on the charged samples. “Feathery” fractures are a distinguishing feature of hydrogen-induced cracking, typically present in low- to medium-strength BCC steels [9,42,69]. Therefore, it is very likely that significant amounts of strain-induced martensite have formed during Slow Strain Rate Testing.

In addition, several fish eyes were found in the vicinity of non-metallic inclusions of type TiN. Fish eyes emerge due to the strong trapping effect within the semi-coherent interface between TiN and the surrounding steel matrix as well as an associated local increase in hydrogen concentration. The corresponding trapping energies are very high, so TiN are referred to as deep traps. Several authors published trapping energies of around 60 kJ/mol [70,71] and even up to around 100 kJ/mol [72]. Therefore, activation of the trapped hydrogen requires either high temperatures or plastic deformation. Since all SSRT in this research has been conducted at room temperature, only plastic deformation is relevant. Due to TiN acting as local stress raisers (notch effect), the interfaces to the steel matrix will tear preliminarily during SSRT. In turn, formerly trapped hydrogen may enter the matrix and contribute to HE.

To better understand the hydrogen-induced failure mode within austenitic stainless steel AISI 321 further investigations such as EBSD in the vicinity of the fracture surface and in particular XRD analyses will be carried out in upcoming work. Therefore, it will be verified whether strain-induced martensite has formed during the SSRT. Other research indicates that HE in AISI 321 is caused by the formation of a BCC phase and localized slipping [73].

The embrittlement indexes of Ni-base alloy IN 625 (material E) were 89% for RRA and 93% for REI, respectively. Both values indicate a good resistance of this alloy to hydrogen embrittlement, although hydrogen contents of around 15 ppm were present within the charged samples. Fractographic investigations revealed localized slipping in the vicinity

of non-metallic inclusions (type TiN). Similar to the existence of fish eyes in the AISI 321 alloy, these findings are explained by the trapping effect of TiN. Once sufficient plastic deformation during SSRT had been reached, the interfaces between TiN and the matrix tore, and trapped hydrogen was activated. However, since these effects have only occurred locally, the overall mechanical behavior of alloy IN 625 was not significantly affected during SSRT.

Ferritic steel 1.4511 (material F) was significantly affected by hydrogen. Both RRA (19%) and REI (51%) indicate that the material only exhibits a mediocre resistance to hydrogen-induced cracking, although no fractures occurred within the elastic region of the stress–strain curve. The hydrogen content within the charged samples was around 0.8 ppm. Fractographic findings confirm the results of SSRT. Significant portions of the fracture surface of the charged samples exhibited a “feathery” pattern, similar to the charged samples of austenitic stainless steel AISI 321. As indicated above, this fracture mode is a distinguishing feature of hydrogen-induced cracking in low- to medium-strength BCC steels such as 1.4511.

Overall, the embrittlement index REI (relative elongation at fracture) was more sensitive than RRA (relative reduction in area) for all Cu-base alloys. However, for alloys AISI 321 and 1.4511 as well as for alloy IN 625, RRA was the more sensitive embrittlement index. These findings should be verified and considered in future work.

4. Discussion and Summary

In the present study, six different metals were investigated with respect to their susceptibility to hydrogen-induced cracking (“hydrogen embrittlement”, HE). The material pool consisted of three high-strength Cu-base alloys with different strengthening mechanisms:

- Alloy 25;
- PerforMet[®];
- ToughMet[®] 3.

In addition, an austenitic stainless steel, a Ni-base alloy, as well as a ferritic stainless steel were tested:

- AISI 321;
- IN 625;
- 1.4511.

Tensile test samples of all materials were charged in pressurized hydrogen until a homogenous hydrogen saturation profile was reached. Subsequently, mechanical tests were carried out by means of Slow Strain Rate Testing (SSRT). The hydrogen contents within the charged samples were analyzed by Thermal Desorption Mass Spectrometry. All results were compared to hydrogen-free reference samples and hydrogen embrittlement indexes RRA (relative reduction in area) and REI (relative elongation at fracture) were calculated. The effect of hydrogen charging on the fracture modes was investigated by fractography within a scanning electron microscope.

The results revealed that high-strength copper Alloy 25 exhibits great resistance to HE. Little to no effects on the mechanical properties were found after hydrogen charging and only small amounts of hydrogen entered the material during pressure charging. Basically, the same holds true for high-strength Cu base alloy PerforMet[®]. However, the elongation at fracture was slightly decreased for the hydrogen-charged samples, but no significant change in fracture morphology was present. The third high-strength Cu alloy, ToughMet[®] 3, was significantly more affected by hydrogen charging. In comparison to the other Cu base alloys, both the hydrogen content within the charged samples was noticeably increased, and the hydrogen embrittlement indexes were lowered. Fractographic investigations revealed an overall decreased plastic deformability in the charged condition.

Further effort will be made to understand the results presented for the high-strength alloy ToughMet[®] 3 (material C), in particular with respect to the increased hydrogen solubility within this alloy. At this point, the authors assume that the findings are related

to the hardening mechanism of spinodal decomposition, which results in high coherency strains due to uniform and high-number-density dispersions of tin-rich perturbations within the Cu matrix [74]. It is known that strain fields increase the hydrogen solubility in metals [75–77]. Since these effects occur to a sub-microscopic extent, spinodally hardened Cu alloys exhibit a multitude of strain fields which increase the hydrogen's solubility.

A second possible explanation is found by additional age hardening that might have taken place during hydrogen charging at 300 °C. Since the uncharged but tempered samples also exhibited altered mechanical properties, temperature-induced microstructural changes are probable. To assess this assumption, additional investigations with the same scope are currently in preparation. Compared to the results presented in this paper, hydrogen charging will be performed at a lower level of 473 K (200 °C).

Austenitic stainless steel AISI 321 was severely affected by hydrogen charging. This is backed up by lowered hydrogen embrittlement indexes as well as distinct fractographic features of hydrogen-induced cracking such as feather-like fracture patterns and “fish eyes”. Similar results with respect to the loss of ductility are reported in [78,79]. Walter et al. confirm that the susceptibility to HE for AISI 321 is comparable to other metastable (i.e., strain-induced martensite forming) ASS such as AISI 304 [80]. Therefore, AISI 321 only exhibits a limited resistance to hydrogen-induced damage.

The same holds true for low-strength ferritic stainless steel 1.4511, which also showed strong indications of hydrogen-induced cracking. In [81], only a few HE effects during slow strain rate testing are reported for this material. However, the same author finds a pronounced decrease in fatigue properties after hydrogen charging. San Marchi et al. report a loss in ductility (elongation at fracture and reduction in area) of around 50% after hydrogen charging [67]. These findings are in good agreement with the results presented in this research.

Ni-base alloy IN 625 performed similarly to Alloy 25 and PerforMet[®] with little to no hydrogen-induced loss in plastic deformability. However, IN 625 was tested in the soft-annelaed condition with a yield strength (YS) of 440 MPa and an ultimate tensile strength (UTS) of around 925 MPa. Both values are significantly lower than those of Alloy 25 (YS: 1100 MPa, UTS: 1240 MPa). The mechanical properties are at the lower end of the specified range for IN 625. Within the literature, a pronounced susceptibility to HE is reported for higher strength levels [82,83].

In summary, the results prove that high-strength Cu base materials Alloy 25 and PerforMet[®] as well as Ni-base alloy IN 625 are suitable materials for hydrogen applications within the frame of the tested parameters. In particular, Alloy 25 offers a large field of applications due to the material's combination of high-strength mechanical properties, low hydrogen solubility and great resistance to HE. In combination with Cu-specific properties such as superior corrosion resistance and (thermal and electric) conductivity, these alloys provide the opportunity to be used in hydrogen applications.

Author Contributions: Conceptualization, J.J., A.F. and K.O.; methodology, J.J. and A.F.; software, not applicable.; validation, J.J., A.F., K.O. and M.P.; formal analysis, J.J., A.F., K.O., S.S. and M.P.; investigation, J.J. and S.S.; resources, A.F., K.O. and M.P.; data curation, J.J. and S.S.; writing—original draft preparation, J.J.; writing—review and editing, J.J., A.F., K.O., S.S. and M.P.; visualization, J.J.; supervision, M.P.; project administration, J.J., A.F., K.O. and M.P.; funding acquisition, A.F., K.O. and M.P. All authors have read and agreed to the published version of the manuscript.

Funding: This research received no external funding.

Data Availability Statement: The data presented in this study are available on request from the corresponding author due to privacy.

Acknowledgments: The authors would like to express their thanks to Theresa Marte (Ruhr-University Bochum, Materials Testing) for supporting the experimental investigations.

Conflicts of Interest: Andreas Frehn and Klaus Ohla (retired) were employed by the Materion Brush GmbH. The remaining authors declare that the research was conducted in the absence of any commercial or financial relationships that could be construed as a potential conflict of interest.

References

1. Song, H.; Luo, S.; Huang, H.; Deng, B.; Ye, J. Solar-driven hydrogen production: Recent advances, challenges, and future perspectives. *ACS Energy Lett.* **2022**, *7*, 1043–1065. [[CrossRef](#)]
2. Cha, J.; Bak, H.; Kwon, I. Hydrogen-fueled CO₂ reduction using oxygen-tolerant oxidoreductases. *Front. Bioeng. Biotechnol.* **2023**, *10*, 1078164. [[CrossRef](#)] [[PubMed](#)]
3. Jürgensen, J.; Pohl, M. Local Hydrogen Measurements in Multi-Phase Steel C60E by Means of Electrochemical Microcapillary Cell Technique. *Metals* **2023**, *13*, 1585. [[CrossRef](#)]
4. Ostadi, M.; Paso, K.G.; Rodriguez-Fabia, S.; Øi, L.E.; Manenti, F.; Hillestad, M. Process Integration of Green Hydrogen: Decarbonization of Chemical Industries. *Energies* **2020**, *13*, 4859. [[CrossRef](#)]
5. Shi, J.; Zhu, Y.; Feng, Y.; Yang, J.; Xia, C. A Prompt Decarbonization Pathway for Shipping: Green Hydrogen, Ammonia, and Methanol Production and Utilization in Marine Engines. *Atmosphere* **2023**, *14*, 584. [[CrossRef](#)]
6. Cho, S.; Kim, G.-I.; Ko, S.-J.; Yoo, J.-S.; Jung, Y.-S.; Yoo, Y.-H.; Kim, J.-G. Comparison of Hydrogen Embrittlement Susceptibility of Different Types of Advanced High-Strength Steels. *Materials* **2022**, *15*, 3406. [[CrossRef](#)] [[PubMed](#)]
7. Gong, P.; Turk, A.; Nutter, J.; Yu, F.; Wynne, B.; Rivera-Diaz-del-Castillo, P.; Rainforth, W.M. Hydrogen embrittlement mechanisms in advanced high strength steel. *Acta Mater.* **2022**, *223*, 117488. [[CrossRef](#)]
8. Ilyushechkin, A.; Schoeman, L.; Carter, L.; Hla, S.S. Material Challenges and Hydrogen Embrittlement Assessment for Hydrogen Utilisation in Industrial Scale. *Hydrogen* **2023**, *4*, 599–619. [[CrossRef](#)]
9. Jürgensen, J.; Pohl, M. Impact and Detection of Hydrogen in Metals. *HTM J. Heat Treat. Mater.* **2023**, *78*, 257–275. [[CrossRef](#)]
10. Li, X.; Ma, X.; Zhang, J.; Akiyama, E.; Wang, Y.; Song, X. Review of Hydrogen Embrittlement in Metals: Hydrogen Diffusion, Hydrogen Characterization, Hydrogen Embrittlement Mechanism and Prevention. *Acta Metall. Sin. (Engl. Lett.)* **2020**, *33*, 759–773. [[CrossRef](#)]
11. Lynch, S.P. Hydrogen embrittlement (HE) phenomena and mechanisms. *Corros. Rev.* **2012**, *30*, 105–112. [[CrossRef](#)]
12. Álvarez, G.; Zafra, A.; Belzunce, F.J.; Rodríguez, C. Effect of Internal Hydrogen on the Fatigue Crack Growth Rate in the Coarse-Grain Heat-Affected Zone of a CrMo Steel. *Metals* **2022**, *12*, 673. [[CrossRef](#)]
13. Tao, P.; Zhou, W.; Miao, X.; Peng, J.; Liu, W. Review of Characterization on Hydrogen Embrittlement by Micro-Sample Testing Methods. *Metals* **2023**, *13*, 1753. [[CrossRef](#)]
14. Michler, T.; Wackermann, K.; Schweizer, F. Review and Assessment of the Effect of Hydrogen Gas Pressure on the Embrittlement of Steels in Gaseous Hydrogen Environment. *Metals* **2021**, *11*, 637. [[CrossRef](#)]
15. Zhang, F.; Wu, Z.; Zhang, T.; Hu, R.; Wang, X. Microstructure Sensitivity on Environmental Embrittlement of a High Nb Containing TiAl Alloy under Different Atmospheres. *Materials* **2022**, *15*, 8508. [[CrossRef](#)] [[PubMed](#)]
16. Ahad, M.T.; Bhuiyan, M.M.H.; Sakib, A.N.; Becerril Corral, A.; Siddique, Z. An Overview of Challenges for the Future of Hydrogen. *Materials* **2023**, *16*, 6680. [[CrossRef](#)] [[PubMed](#)]
17. Atrens, A.; Gray, E.; Venezuela, J.; Hoschke, J.; Roethig, M. Feasibility of the Use of Gas Phase Inhibition of Hydrogen Embrittlement in Gas Transmission Pipelines Carrying Hydrogen: A Review. *Jom* **2022**, *75*, 232–238. [[CrossRef](#)]
18. Earnshaw, A.; Greenwood, N.N. *Chemistry of the Elements*, 2nd ed.; Butterworth-Heinemann: Oxford, UK, 1997; ISBN 0750633654.
19. Fukuyama, S.; Yokogawa, K. *Pressure Vessel Technology*, 2nd ed.; Verband der Technischen Überwachungs-Vereine: Essen, Germany, 1992; pp. 914–923.
20. Srikrishnan, V.; Ficalora, P.J. The Role of Gaseous Impurities in Hydrogen Embrittlement of Steel. *J. Vac. Sci. Technol.* **1977**, *14*, 588–592. [[CrossRef](#)]
21. Zhou, C.; He, Y.; Jiang, J.; Zhang, K.; Tang, D.; Zhu, H.; Shang, J.; Sun, G.; Wang, M.; Zhang, L.; et al. Hydrogen uptake induced by CO₂ enhances hydrogen embrittlement of iron in hydrogen blended natural gas. *Corros. Sci.* **2022**, *207*, 110594. [[CrossRef](#)]
22. Li, Q.; Ghadiani, H.; Jalilvand, V.; Alam, T.; Farhat, Z.; Islam, M.A. Hydrogen Impact: A Review on Diffusibility, Embrittlement Mechanisms, and Characterization. *Materials* **2024**, *17*, 965. [[CrossRef](#)]
23. Metalnikov, P.; Ben-Hamu, G.; Eliezer, D. Hydrogen Trapping in Laser Powder Bed Fusion 316L Stainless Steel. *Metals* **2022**, *12*, 1748. [[CrossRef](#)]
24. Van den Eeckhout, E.; Depover, T.; Verbeken, K. The Effect of Microstructural Characteristics on the Hydrogen Permeation Transient in Quenched and Tempered Martensitic Alloys. *Metals* **2018**, *8*, 779. [[CrossRef](#)]
25. Depover, T.; Laureys, A.; Pérez Escobar, D.; Van den Eeckhout, E.; Wallaert, E.; Verbeken, K. Understanding the Interaction between a Steel Microstructure and Hydrogen. *Materials* **2018**, *11*, 698. [[CrossRef](#)]
26. Shen, X.; Song, W.; Sevsek, S.; Ma, Y.; Hüter, C.; Spatschek, R.; Bleck, W. Influence of Microstructural Morphology on Hydrogen Embrittlement in a Medium-Mn Steel Fe-12Mn-3Al-0.05C. *Metals* **2019**, *9*, 929. [[CrossRef](#)]
27. Riecke, E.; Bohnenkamp, K. Über den Einfluß von Gitterstörstellen in Eisen auf die Wasserstoffdiffusion. *Z. Met.* **1984**, *75*, S76–S81. [[CrossRef](#)]
28. Gibala, R.; DeMiglio, D.S. Hydrogen in iron and steels: Interactions, traps and crack path. In *Hydrogen Effects in Metals*; Bernstein, I.M., Thompson, A.W., Eds.; The Metallurgical Society of AIME: Warrendale, PA, USA, 1980.

29. Pressouyre, G.M. Trap theory of hydrogen embrittlement: Experimental investigations. In *Hydrogen Effects in Metals*; Bernstein, I.M., Thompson, A.W., Eds.; The Metallurgical Society of AIME: Warrendale, PA, USA, 1980.
30. Kholobina, A.S.; Pippin, R.; Romaner, L.; Scheiber, D.; Ecker, W.; Razumovskiy, V.I. Hydrogen Trapping in bcc Iron. *Materials* **2020**, *13*, 2288. [[CrossRef](#)] [[PubMed](#)]
31. Zhou, C.; Ren, Y.; Yan, X.; Zheng, Y.; Liu, B. A Bibliometric and Visualized Overview of Hydrogen Embrittlement from 1997 to 2022. *Energies* **2022**, *15*, 9218. [[CrossRef](#)]
32. Birnbaum, H.K.; Sofronis, P. Hydrogen-enhanced localized plasticity—A mechanism for hydrogen-related fracture. *Mater. Sci. Eng. A* **1994**, *17*, 191–202. [[CrossRef](#)]
33. Brück, S.; Schippl, V.; Schwarz, M.; Christ, H.-J.; Fritzen, C.-P.; Weihe, S. Hydrogen Embrittlement Mechanism in Fatigue Behavior of Austenitic and Martensitic Stainless Steels. *Metals* **2018**, *8*, 339. [[CrossRef](#)]
34. Troiano, A.R. The role of hydrogen and other interstitials in the mechanical behavior of metals. *Metallogr. Microstruct. Anal.* **2016**, *5*, 557–569. [[CrossRef](#)]
35. Dear, F.F.; Skinner, G.C.G. Mechanisms of hydrogen embrittlement in steels: Discussion. *Philos. Trans. R. Soc. A* **2017**, *375*, 20170032. [[CrossRef](#)] [[PubMed](#)]
36. Lynch, S.P. Progress towards understanding mechanisms of hydrogen embrittlement and stress corrosion cracking. In Proceedings of the CORROSION 2007, Nashville, TN, USA, 11–15 March 2007; pp. 074931–074935.
37. Lynch, S.P. Environmentally assisted cracking: Overview of evidence for an adsorption-induced localised-slip process. *Acta Metall.* **1988**, *36*, 2639–2661. [[CrossRef](#)]
38. Nagumo, M. Hydrogen related failure of steels—A new aspect. *Mater. Sci. Technol.* **2004**, *20*, 940–950. [[CrossRef](#)]
39. Paxton, T.; Frs, A.P.S.; Finnis, M.W. The challenges of hydrogen and metals. *Philos. Trans. R. Soc. A Math. Phys. Eng. Sci.* **2017**, *375*, 20170198. [[CrossRef](#)] [[PubMed](#)]
40. Pohl, M. Failure Analysis to Clarify Unambiguous Hydrogen Fracturing in Steels. *Metallogr. Microstruct. Anal.* **2017**, *6*, 282–288. [[CrossRef](#)]
41. Pöpperling, R.K. Wasserstoff-induzierte Rißbildung an unlegierten und niedriglegierten Stählen. In *Wasserstoff und Korrosion*, 2nd ed.; Kuron, D., Ed.; Verlag Irene Kuron: Bonn, Germany, 2000; pp. 54–72.
42. Jürgensen, J.; Pohl, M. Differenzierende Wasserstoffanalytik zum Nachweis von Wasserstoffversprödung. In *Tagungsband zur “Tagung Werkstoffprüfung 2021—Werkstoffe und Bauteile auf dem Prüfstand”*; Brockmann, S., Krupp, U., Eds.; Stahlinstitut VDEh: Düsseldorf, Germany, 2021.
43. Olson, P.; Bauer, A.D.; Eriksson, H. Duplex Stainless Steels 97. In Proceedings of the 5th World Conference, Maastricht, The Netherlands, 21–23 October 1997; pp. 607–618.
44. Böllinghaus, T.; Kannengießer, T. *Supermartensitic Stainless Steels 2002*; KCI Publishing B.V.: Deventer, The Netherlands, 2002; pp. 71–76.
45. Adenna, C.; Torella, R. Hydrogen Transport and Cracking in Metals. In Proceedings of the NPL, Teddington, UK, 13–14 April 1994.
46. Gorsky, W.S. Theorie der elastischen Nachwirkung in ungeordneten Mischkristallen (elastische Nachwirkung zweiter Art). *Phys. Z. Sowjetunion* **1935**, *8*, 457–471.
47. Holstein, N.; Krauss, W.; Nitti, F.S. Development and Basic Qualification Steps towards an Electrochemically Based H-Sensor for Lithium System Applications. *J. Nucl. Eng.* **2023**, *4*, 1–10. [[CrossRef](#)]
48. Smith, L.; Celant, M.; Pourbaix, A. *Duplex America 2000 Conference: Stainless Steel World*; KCL Publishing: London, UK, 2000.
49. Pircher, H.; Großterlinden, R. Wasserstoffinduzierte Korrosion von niedriglegierten Stählen in wässrigen Medien. *Werkst. Korros.* **1987**, *38*, 57–64. [[CrossRef](#)]
50. Izawa, C.; Wagner, S.; Deutges, M.; Martín, M.; Weber, S.; Pargeter, R.; Michler, T.; Uchida, H.-H.; Gemma, R.; Pundt, A. Relationship between hydrogen embrittlement and M_d30 temperature: Prediction of low-nickel austenitic stainless steel’s resistance. *Int. J. Hydrogen Energy* **2019**, *44*, 25064–25075. [[CrossRef](#)]
51. Choi, Y.-H.; Lee, J.H.; Kim, S.-M.; Lee, D.-H.; Kim, H.-T.; Kim, J.-H.; Kim, M.; Kim, S.-K.; Lee, J.-M. Temperature-Dependent Hydrogen Embrittlement of Austenitic Stainless Steel on Phase Transformation. *Metals* **2023**, *13*, 35. [[CrossRef](#)]
52. Gibbs, P.J.; Hough, P.D.; Thurmer, K.; Somerday, B.P.; San Marchi, C.W.; Zimmerman, J.A. Stacking Fault Energy Based Alloy Screening for Hydrogen Compatibility. *JOM. J. Miner. Met. Mater. Soc.* **2020**, *72*, 1982–1992. [[CrossRef](#)]
53. Michler, T.; Bruder, E.; Lindner, S. Hydrogeneffects in X30MnCrN16-14 austenitic steel. *Mater. Werkst.* **2020**, *51*, 531–538. [[CrossRef](#)]
54. Astafurova, E.; Fortuna, A.; Melnikov, E.; Astafurov, S. The Effect of Strain Rate on Hydrogen-Assisted Deformation Behavior and Microstructure in AISI 316L Austenitic Stainless Steel. *Materials* **2023**, *16*, 2983. [[CrossRef](#)] [[PubMed](#)]
55. Weber, S.; Martin, M.; Theisen, W. Impact of heat treatment on the mechanical properties of AISI 304L austenitic stainless steel in high-pressure hydrogen gas. *J. Mater. Sci.* **2012**, *47*, 6095–6107. [[CrossRef](#)]
56. Michler, T.; Bruder, E. Local strains in 1.4301 austenitic stainless steel with internal hydrogen. *Mater. Sci. Eng. A* **2018**, *725*, 447–455. [[CrossRef](#)]
57. Butomo, D.G.; Zedin, N.I.; Mnushkin, O.S. Effect of oxygen on the susceptibility of copper to “hydrogen sickness”. *Met. Sci. Heat Treat.* **1968**, *10*, 184–185. [[CrossRef](#)]
58. Pohl, M. Hydrogen in Metals: A Systematic Overview. *Pract. Metallogr.* **2014**, *51*, 291–305. [[CrossRef](#)]
59. Yamabe, J.; Takagoshi, D.; Matsunaga, H.; Matsuoka, S.; Ishikawa, T.; Ichigi, T. High-strength copper-based alloy with excellent resistance to hydrogen embrittlement. *Int. J. Hydrogen Energy* **2016**, *41*, 15089–15094. [[CrossRef](#)]

60. Eichenauer, W.; Löser, W.; Witte, H. Löslichkeit und Diffusionsgeschwindigkeit von Wasserstoff und Deuterium in Einkristallen aus Nickel und Kupfer. *Int. J. Mater. Res.* **1965**, *56*, 287–293. [[CrossRef](#)]
61. Katz, L.; Guinan, M.; Borg, R.J. Diffusion of H₂, D₂, and T₂ in single-crystal Ni and Cu. *Phys. Rev. B* **1971**, *4*, 330. [[CrossRef](#)]
62. Caskey, G.R.; Dexter, A.H.; Holzworth, M.L.; Louthan, M.R.; Derrick, R.G. The Effect of Oxygen on Hydrogen Transport in Copper. *Corrosion* **1976**, *32*, 370–374. [[CrossRef](#)]
63. Begeal, D.R. Hydrogen and Deuterium Permeation in Copper Alloys, Copper-Gold Brazing Alloys, Gold, and the in-situ Growth of Stable Oxide Permeation Barriers. *J. Vac. Sci. Technol.* **1978**, *15*, 1146–1154. [[CrossRef](#)]
64. Ishikawa, T.; McLellan, R.B. The diffusivity of hydrogen in copper at low temperatures. *J. Phys. Chem. Solids* **1985**, *46*, 445–447. [[CrossRef](#)]
65. DIN EN 10088-3:2014-12; Stainless Steels—Part 3: Technical Delivery Conditions for Semi-Finished Products, Bars, Rods, Wire, Sections and Bright Products of Corrosion Resisting Steels for General Purposes. Beuth Verlag GmbH: Berlin, Germany, 2014.
66. DIN 50125:2022-08; Testing of Metallic Materials—Tensile Test Pieces. Beuth Verlag GmbH: Berlin, Germany, 2022.
67. San Marchi, C.W.; Somerday, B.P. *Technical Reference on Hydrogen Compatibility of Materials*; Sandia Report SAND2012-7321; Sandia National Laboratories (SNL): Albuquerque, NM, USA; Livermore, CA, USA, 2012.
68. San Marchi, C.; Somerday, B.P.; Robinson, S.L. Permeability, solubility and diffusivity of hydrogen isotopes in stainless steels at high gas pressures. *Int. J. Hydrogen Energy* **2007**, *32*, 100–116. [[CrossRef](#)]
69. Sofronis, P.; Robertson, I.M. A Combined Materials Science/Mechanics Approach to the Study of Hydrogen Embrittlement of Pipeline Steels. In *2011 DOE Hydrogen and Fuel Cells Program Review*; University of Illinois: Champaign, IL, USA, 2011.
70. Wei, F.G.; Tsuzaki, K. Quantitative analysis on hydrogen trapping of TiC particles in steel. *Metall. Mater. Trans. A* **2006**, *37*, 331–353. [[CrossRef](#)]
71. Lee, H.G.; Lee, J.-Y. Hydrogen trapping by TiC particles in iron. *Acta Metall.* **1984**, *32*, 131–136. [[CrossRef](#)]
72. Kawakami, K.; Matsumiya, T. Numerical Analysis of Hydrogen Trap State by TiC and V₄C₃ in bcc-Fe. *ISIJ Int.* **2012**, *52*, 1693–1697. [[CrossRef](#)]
73. Tyson, W.R. The effect of lattice defects on hydrogen solubility. *J. Less Common Met.* **1980**, *70*, 209–212. [[CrossRef](#)]
74. Cribb, W.R. Copper Spinodal Alloys for Aerospace. *Adv. Mater. Processes* **2006**, *164*, 44.
75. Zhou, H.-B.; Jin, S.; Zhang, Y.; Lu, G.-H. Anisotropic Strain Enhanced Hydrogen Solubility in bcc Metals: The Independence on the Sign of Strain. *Phys. Rev. Lett.* **2012**, *109*, 135502. [[CrossRef](#)]
76. Psiachos, D.; Hammerschmidt, T.; Drautz, R. Ab initio study of the modification of elastic properties of alpha-iron by hydrostatic strain and by hydrogen interstitials. *Acta Mater.* **2011**, *59*, 4255. [[CrossRef](#)]
77. Connétable, D.; Maugis, P. Hydrogen diffusivity and solubility in stressed fcc crystals. *J. Alloys Compd.* **2021**, *879*, 160425. [[CrossRef](#)]
78. Cai, W.; Wang, Z.; Liang, Q.; Zhu, Z.; Wang, F.; Fu, Y.; He, W. Enhancing Hydrogen Embrittlement Resistance of AISI 321 Austenitic Stainless Steel through Yttrium Addition: Exploring the Influence on Microstructure and Precipitates. Available online: <https://ssrn.com/abstract=4768837> (accessed on 26 March 2024). [[CrossRef](#)]
79. Xiuqing, X.; Junwei, A.; Chen, W.; Jing, N. Study on the hydrogen embrittlement susceptibility of AISI 321 stainless steel. *Eng. Fail. Anal.* **2021**, *122*, 105212. [[CrossRef](#)]
80. Walter, R.J.; Hayes, H.G.; Chandler, W.T. *Influence of Gaseous Hydrogen on Metal*; Report N-71-32489; Marshall Space Flight Center: Huntsville, AL, USA, 1971.
81. Schauer, G. *Auslegungsansatz für Stahlbauteile bei Ermüdungsbeanspruchung in Druckwasserstoffatmosphäre*; Technisch-Wissenschaftlicher-Bericht Band: 2018/02; MPA Universität Siegen: Siegen, Germany, 2018.
82. Hicks, P.; Altstetter, C. Comparison of Internal Hydrogen Embrittlement of Superalloys 718 and 625. *Superalloys* **1991**, *718*, 635–651.
83. Daum, R.S.; Motta, A.T.; Koss, D.A. Hydrogen-Assisted Failure of Alloys X-750 and 625 Under Slow Strain-Rate Conditions. In *Ninth International Symposium on Environmental Degradation of Materials in Nuclear Power Systems—Water Reactors*; John Wiley & Sons: Hoboken, NJ, USA, 1999. [[CrossRef](#)]

Disclaimer/Publisher’s Note: The statements, opinions and data contained in all publications are solely those of the individual author(s) and contributor(s) and not of MDPI and/or the editor(s). MDPI and/or the editor(s) disclaim responsibility for any injury to people or property resulting from any ideas, methods, instructions or products referred to in the content.